NUMERICAL INVESTIGATION OF THE ORIGIN OF VORTEX ASYMMETRY
OF FLOWS OVER BODIES AT LARGE ANGLE OF ATTACK

David Degani*

NASA Ames Research Center

Moffett Field, CA. 94035

Abstract

The phenomena of the flow about a slender body of revolution placed at incidence to an oncoming stream were numerically investigated for angles of attack ranging from 20° to 80°, and a Reynolds number of 200,000 based on maximum body diameter. At angle of attack of 20° the flow was steady and symmetric, and the presence of a perturbation which was placed near the tip of the body made only a small change. At angle of attack of 40° the flow was found to be steady (except for a small-amplitude, high-frequency unsteadiness of the shear-layer), but became highly asymmetric when a space-fixed, time-invariant disturbance was added near the tip. The level of the asymmetry was dependent upon the size and location of the disturbance. When the disturbance was removed the flowfield relaxed to its original symmetric shape. On the basis of this observation and other theoretical indicators, it is suggested that the origin of the asymmetry is a convective-type instability of the originally symmetric flow.

For higher angles of attack ($\alpha = 60°$ and $\alpha = 80°$) the flow around the cylindrical part of the body became unsteady and vortex shedding was observed. For the 80° case the corresponding Strouhal frequency was about 0.2 which is in agreement with the average value of the Strouhal frequency for flow around a two-dimensional cylinder under the same oncoming flow condition. For both angles of attack, ($\alpha = 60°$ and $\alpha = 80°$) a small temporal disturbance of finite duration was sufficient to trigger the unsteadiness, which evolved to a finite amplitude fluctuation in the wake. On the basis of this observation and other theoretical indicators, it is suggested that the origin of flow unsteadiness and vortex-shedding in the wake is an absolute-type instability of the originally steady flow. When a permanent disturbance was also added near the tip of the body in the case of 60° angle of attack, a pair of asymmetric vortices emerged from the vicinity of the body nose. Just as in the case of $\alpha = 40°$, it is suggested that these vortices are the results of a convective-type instability of the originally symmetric flow and thus it appears that both types of instability can coexist.

* National Research Council Senior Research Associate. Associate Professor, Technion IIT, Faculty of Mechanical Engineering.

Introduction

The flow observed about a slender body of revolution placed at incidence to an oncoming stream exhibits a wide variety of phenomena[1-4]. As the angle of attack is increased from zero, a steady, symmetric pair of vortices is observed in the leeward-side flow. With further increase in incidence, the symmetric vortex pair becomes asymmetric, but the flow remains steady in time. At still higher incidence, the steady asymmetric flow evolves to a steady pattern of multiple vortices that leave from alternate sides of the body with increasing distance downstream. With further increase in incidence, the asymmetric flow becomes nonsteady, and, as the angle of attack tends toward 90°, the flow pattern approaches that of a circular cylinder in crossflow (except for the region near the nose). Vortices are shed periodically from alternate sides of the cylinder and are convected downstream to form the classic Karman vortex street.

Time-accurate computations of two-dimensional flow about a circular cylinder[5-7] (using algorithms that are unbiased in the circumferential direction) have revealed that, unless a symmetry-breaking perturbation was introduced into the flow, the solutions remained symmetric and steady. The perturbations were typically introduced for a short period of time, then removed, and the flows advanced in time until the oscillatory solution was developed.

The mechanisms which lead to an asymmetric vortex wake in three-dimensional flow are not well understood at the present time. Several mechanisms for laminar and fully turbulent flows[8-9] and for transitional flows[10] have been advanced. First, it has been suggested that the asymmetry is a result of an instability of the flow in the crossflow planes above the body. Second, it has been suggested that the asymmetry occurs due to an asymmetric transition of the boundary-layer flow.

In Refs. 11-13, a time-accurate thin-layer Navier-Stokes code[14] was utilized to study the three dimensional, subsonic laminar flow surrounding a slender body of revolution at large incidence. Computed results for the flow surrounding an ogive-cylinder at $M_\infty = 0.2$, $\alpha = 40°$, and Reynolds number (based on free-stream conditions and cylinder diameter) $Re_D = 200,000$ indicated that the computed flow remained symmetric at angles of attack where experimental measurements showed the presence of large asymmetry. Guided by the results for the two-dimensional cylinder flow, the authors applied a transient symmetry-breaking perturbation to induce asymmetry. When the perturbation (a small surface jet blowing normal to the surface and perpendicular to the angle-of-attack plane) was introduced, the solution started to evolve to an asymmetric

state. If the jet was kept on at constant strength, the computed flow reached and maintained an asymmetric state. However, in contrast to the results of the computations for two-dimensional vortex shedding, when the jet was turned off[13], the asymmetry in the flow began to dissipate and the flow returned to a symmetric state as demonstrated in Fig. 1.

In the current work Navier-Stokes computations have been applied to further investigate the phenomena governing the onset of vortex asymmetry. To more realistically simulate the body surface boundary conditions, the jet that was used previously was replaced by a small geometrical disturbance. Time-accurate solutions were obtained for flow over an ogive-cylinder body, for angles of attack ranging from $\alpha = 20°$ to $\alpha = 80°$ and a Reynolds number (based on free-stream conditions and cylinder diameter) $Re_D = 200,000$.

Theoretical Background

Governing Equations

The conservation equations of mass, momentum, and energy can be represented in a flux-vector form that is convenient for numerical simulation as[15]

$$\partial_\tau \hat{Q} + \partial_\xi (\hat{F} + \hat{F}_v) + \partial_\eta (\hat{G} + \hat{G}_v) + \partial_\zeta (\hat{H} + \hat{H}_v) = 0 \quad (1)$$

where τ is the time and the independent spatial variables, ξ, η, and ζ are chosen to map a curvilinear body-conforming grid into a uniform computational space. In Eq. (1) $\hat{Q}$ is the vector of dependent flow variables; $\hat{F} = \hat{F}(\hat{Q})$, $\hat{G} = \hat{G}(\hat{Q})$, and $\hat{H} = \hat{H}(\hat{Q})$ are the inviscid flux vectors, while the terms $\hat{F}_v$, $\hat{G}_v$, and $\hat{H}_v$ are fluxes containing the viscous derivatives. A nondimensional form of the equations is used throughout this work. The conservative form of the equations is maintained chiefly to capture the Rankine-Hugoniot shock jump relations (where applicable) as accurately as possible.

For body-conforming coordinates and high-Reynolds number flow, if ζ is the coordinate leading away from the surface, the thin-layer approximation can be applied, which yields[16,17]

$$\partial_\tau \hat{Q} + \partial_\xi \hat{F} + \partial_\eta \hat{G} + \partial_\zeta \hat{H} = Re^{-1} \partial_\zeta \hat{S} \quad (2)$$

where only viscous terms in ζ are retained. These have been collected into the vector $\hat{S}$ and the nondimensional Reynolds number Re is factored from the viscous flux term.

Numerical Algorithm

The implicit scheme employed in this study is the algorithm reported by Steger et al in Ref. 14. The algorithm uses flux-vector splitting[18] and upwind spatial differencing for the convection terms in one coordinate direction (nominally streamwise). As discussed in Ref. 14, schemes using upwind differencing can have several advantages over methods which utilize central spatial differences in each direction. In particular, such schemes can have natural numerical dissipation and better stability properties. By using upwind differencing for the convective terms in the streamwise direction while retaining central differencing in the other directions, a two-factor implicit approximately-factored algorithm is obtained. Additional details of the numerical algorithm can be found in Ref. 14.

Body Configurations and Computational Grids

Computations were performed for subsonic flow over an ogive-cylinder body, which consisted of a 3.5 diameter tangent ogive forebody with a 7.0 diameter cylindrical afterbody extending aft of the nose-body junction to x/D = 10.5. The grid consisted of 120 equispaced circumferential planes ($\Delta\phi = 3°$) extending completely around the body. In each circumferential plane the grid contained 50 radial points between the body surface and the computational outer boundary, and 59 axial points between the nose and the rear of the body (Fig. 2). This grid spacing was found adequate for similar flowfields in previous calculations[11,12,13].

Boundary Conditions and Initial Conditions

An adiabatic no-slip boundary condition was applied at the body surface, while undisturbed free-stream conditions were maintained at the computational outer boundary. An implicit periodic continuation condition was imposed at the circumferential edges of the grid, while at the downstream boundary a simple zero-axial-gradient extrapolation condition was applied. This simple extrapolation boundary condition is not strictly valid in subsonic flow, since the body wake can affect the flow on the body. However, by letting both computed body lengths extend beyond the physical length of the experimental model[3,4], and by neglecting the portion of the flow near the downstream boundary, the effect of the boundary can be minimized. On the upstream axis of symmetry an extrapolation boundary condition was used to obtain the flow conditions on the axis from the cone of points one axial plane downstream.

In these computations, a time-accurate solution was required. Thus, the second-order time-accurate algorithm was used with a globally-constant time step. The flowfield was initially set to free-stream conditions throughout the grid, or to a previously obtained solution, and the flowfield was advanced in time until a solution was obtained.

A small geometrical bump was added to the body surface to act as a symmetry-breaking perturbation (Fig.3). The height of the bump ranged from 0.005 to 0.02 of the body diameter, the length of the bump was 0.05 of the body diameter and it was located at x/D $\approx$ 0.025 and 90° circumferentially from the windward meridian.

The code required approximately 8×10^{-5} sec/iteration/grid point on the NAS CRAY-2 computer. This translates to approximately 27 sec/iteration. Further, the need to resolve the thin viscous layers for high-Reynolds-number flow required that the grid have a fine radial spacing at the body surface. As a result, the allowable computational nondimensional time steps were found to range from 0.008 to 0.010.

Results

At a low angle of attack, $\alpha = 20°$, the flow as observed experimentally[3,4,9,19,20] is almost symmetric. Results of previous computations[11-13,21] for this angle of attack were perfectly symmetric and agreed very well with experimental results[9]. To test the effect of roughness at low angles of attack, a small geometrical perturbation was introduced as explained above, with h/D=0.02. Although the size of the perturbation in this case is not negligible (twice the size of the maximum perturbation which was used for other cases), the change in the flow is small. This is demonstrated in Fig. 4 which presents computed circumferential surface pressure coefficient distributions against experimental data[9] for two axial locations. It can be seen from Fig. 4 that the agreement between the computed and measured pressures is very good for both stations. Figure 5 shows the effect of the perturbation on the side force coefficient as a function of time. The maximum value of the side force coefficient is less than 5% of the normal force coefficient. The vortical flowfield above the body has very little asymmetry as can be seen in Fig. 6. Figure 6a shows the computed helicity density contours in several cross sections along the body. (Helicity density is defined as the scalar product of the local velocity and vorticity vectors. Since it indicates both the strength and sense of rotation of the vortices, helicity density has been found to be an excellent means of visualizing the position and strength of the vortex pattern[22,23]. By marking positive and negative values of helicity with different colors it is easy to differentiate between the primary and secondary vortices). Only small differences can be observed between the two primary vortices on both sides of the body. The corresponding off-surface streamline pattern (Fig. 6b) shows the presence of a pair of almost symmetric primary vortices. The vortices are almost parallel and close to the upper body surface.

Previous computations[11-13] showed that even for an angle of attack of 40° the computed flow remains symmetric and is stable to small, temporal perturbations. Figure 7 shows the off-surface streamline pattern for this symmetric case. The two vortices which originate at the nose run almost parallel to the body upper surface as they grow with distance downstream. In contrast to experimental observations[3,4,19,20,24] the computed vortices do not appear to curve away from the body surface.

It has been already suggested (cf. eg. Refs. 12,13,19,20,24) that vortex asymmetry originates from imperfections of the nose. It was also demonstrated[12,13] that it is essential to introduce a space-fixed, time invariant perturbation (a small jet in Refs. 12-13) into the computation to simulate the imperfection. In the current work, to simulate the physics more realistically, rather than using a jet, a geometrical perturbation was added to the body at $x/D \approx 0.025$ and with maximum height of h/D=0.01 (Fig.3). Figure 8 demonstrates the dramatic change in the flowfield that resulted from the perturbation. The flowfield became highly asymmetric, as shown in the helicity density contours in Fig. 8a. The corresponding off-surface streamline pattern (Fig. 8b) shows the presence of two pairs of primary vortices. The upstream pair is highly asymmetric and the vortices curve away from the body surface about one and a half body diameters from the tip (the dashed lines represent streamlines on the far side of the body). Upstream of the point when the vortices lift off, the change

of the streamline pattern between both sides of the body is very moderate. This can be seen by comparing Fig. 8b to Fig. 7. The flow asymmetry in the vicinity of the geometric disturbance is very small but grows nonlinearly beyond the point where the vortices lift off. Downstream, the vortices are not parallel to the free stream but are inclined approximately 5° toward the body from the freestream direction. The second pair of vortices run almost parallel to the body surface but they start to lift off near the aft end of the body. When the disturbance was removed, the flowfield relaxed back to a symmetric state, as was previously demonstrated for the jet in the earlier studies[11-13].

It was found experimentally (cf. Refs. 3,4,9,19-20,24) that at angle of attack of 40°, as the size or the location of the disturbance changed, the position of the first pair of primary vortices changed in what appeared to be an arbitrary way, sometimes even to the extent of becoming almost symmetric. It was also observed that for a given configuration there was a maximum extent of vortex asymmetry such that an increase in the level of the disturbance did not further increase the extent of asymmetry.

In order to test the latter finding computationally, the size of the geometrical perturbation was cut to one half of the original size (ie, h/D=0.005). The computational results show a decrease in the extent of asymmetry and a change in sign of the total side force coefficients, as shown in Figs. 9 and 10.

Figure 9 presents the time history of side force coefficients for the last two cases, ie, for $\alpha = 40°$, with two sizes of disturbances, h/D=0.01 (solid line) and h/D=0.005 (dashed line, which was started at a nondimensional time of $\bar{t} = 32$). The side-force coefficients for the second case converge toward a positive value, while in the case of h/D=0.01, the side force coefficients fluctuate around a negative mean value. Figure 10 shows the off-surface streamline pattern for the case of h/d=0.005. In comparison to Fig. 8b, the first two primary vortices are positioned lower above the body upper surface and the asymmetry is smaller in extent. It is also evident that the vortex on the far side of the body (marked by dashed lines) is higher than the one on the near side (where the disturbance is located). This may explain why the side force coefficients are positive for this case, while in the case of h/D=0.01 the side force coefficients are negative. Since both cases present high levels of unsteadiness due to the large laminar Reynolds number, and since the solutions probably have not reached their equilibrium states, it is hard to draw a firm conclusion.

Experiments[3,4,25] showed that at angles of attack larger than 55° − 60° the flowfield presented significant amount of unsteadiness due to vortex shedding of the flow in the wake of the cylindrical portion of the body. Vortex shedding from a cylinder can be described as a phenomenon involving absolute instability, which means that in order to move the flowfield from an unstable symmetric wake to a self-sustained oscillation of the wake, it is sufficient to introduce a short perturbation in time.

To test this computationally, a case was initiated for $\alpha = 60°$, with the initial solution of the symmetric $\alpha = 40°$ case. A small change of the density was imposed in a small volume on one side of the body near the tip. The perturbation was removed after the total side force (which was zero at the beginning of the process) became about 5% of

the total normal force (at $\bar{t} = 32$). The flowfield continued to evolve to an unsteady oscillating one. The solid line in Fig. 11 presents the time history of the side force coefficient of this development. Obviously the total computed time is too short in terms of physical time to draw final conclusions but it is clear that the flow is instantaneously highly asymmetric even without the presence of a permanent perturbation, but is fluctuating around a symmetric mean. From Fig. 12, which shows the helicity density contours and the corresponding off-surface instantaneous streamlines, the fact that the flowfield is highly asymmetric becomes more evident. The reader should note that since the flowfield is unsteady the instantaneous streamlines shown in Fig. 12b do not represent particle traces and should not be interpreted as such. By comparing Fig. 12 to the case of $\alpha = 40°$ (Fig. 8), one can note a significant difference: the first pair of primary vortices which curve away from the nose for the $\alpha = 40°$ case, do not lift off for the $\alpha = 60°$ case but rather stay parallel to the body upper surface and ultimately curve away only on the aft part of the body. It also evident that all four vortices interact with each other in a relatively small space above the aft part of the body. As a result, the instantaneous streamlines do not form tight vortices but are scattered. It was also found that all vortices change their position with time and move with small amplitude back and forth possibly in correlation with the change in the side force.

From experimental observations[3,4,24] for angle of attack of $\alpha = 60°$, it was expected that the first pair of vortices would lift off near the tip. It seemed possible that in order to excite the tip vortices, a space-fixed perturbation was needed. Accordingly, another computational experiment was conducted by adding a geometrical disturbance (h/D=0.01) at x/D $\approx$ 0.005 and the computations continued using the previous solution as an initial solution. The dashed line in Fig. 11 shows the time history of this case. The flow is still oscillatory with large force side amplitudes. However, a significant change is evident from the helicity contours and the corresponding off-surface instantaneous streamlines (Fig. 13). Immediately after the disturbance was added a relatively weak vortex shot up near the tip on the side of the nose where the disturbance was mounted. Later, after a development that took $\bar{t} = 25$ (which is about the time for a particle in the flow to travel three body lengths) a second and stronger vortex lifted off on the other side of the nose. Correspondingly, the fluctuating flow developed an asymmetric mean component (as can be seen from Fig. 11). At the same time, the vortices above the cylindrical afterbody continued to be unsteady in a similar manner to the unsteadiness that existed before the permanent disturbance was introduced near the tip. Here, again, the instantaneous streamlines above the aft portion of the body do not form tight vortices; they fill the whole space between the body and the second primary vortex, and they move back and forth with time.

For technical reasons the cylindrical portion of the body in the case of $\alpha = 80°$ is shorter than the one of other cases (L/D=6.5). From experiment[3,4] it is known that at this angle of attack the flow about the cylindrical portion of the body should be fluctuating at a Strouhal number of about 0.21 (which is the Strouhal number of flow around a two-dimensional cylinder under the same flow conditions). The computations were started from uniform free stream flow. A short time perturbation, similar to the one used for the $\alpha = 60°$ case, was imposed. The flowfield very rapidly became asymmetric and oscillatory. Figure 14 shows the time history of the side force coefficient for this case. It is obvious that vortices are being shed but in an irregular manner. This is due in part to the relatively short time since the flow was started from rest, to the high laminar Reynolds number of the flow, to high-frequency riders and to three-dimensional effects of the short body. Nevertheless, Fourier analysis of the time history shows that aside from the high-frequency riders, the equivalent Strouhal number for the dominant frequency is about 0.2. Figure 15 shows four snapshots of helicity density contours at several cross sections of the flowfield. These snapshots represent about one cycle of the low frequency oscillation. Since the figure is in black and white, at the last station each vortex cross section is marked with + or - to indicate the direction of the rotation of the vortex. By following one vortex as it develops with time, for example the one which is marked ℵ in Fig. 15a, it is clear that the vortex moves upward in time and a new one starts to build up under it. Figure 16 shows a close-up of the downstream cross-section of Fig. 15, in the area near the cylinder surface. The unsteadiness of the shear-layer can be clearly seen as small vortices move along the shear layer and merge into the primary vortex: A small vortex is formed in the shear-layer (marked as '1'), moves upward and merges into the primary vortex above it. Meanwhile a new vortex is forming below it (marked as '2' in Fig. 16d). This unsteadiness is probably responsible for the high frequency riders that appear in the time history of the side force.

Discussion and Conclusions

The computational results presented in this paper and experimental findings (cf. Refs. 3,4,19,20,24,25), suggest that, at least over a certain range of Reynolds numbers, the trend of flowfields around slender bodies at incidence can be roughly divided into three main groups (and the range of incidence for each group may change by $\pm 10°$, depending on the quality of flow, body finish, etc):

Range I: $0° < \alpha < 30°$. In this range of angles of attack the flow is steady and symmetric. At angles of attack above 10° (depending on flow conditions and the forebody shape) a pair of symmetric vortices appears and runs almost parallel to the body upper surface. Introduction of small disturbances near the tip (or at other locations along the body) has only a small effect on the symmetry of the flow and the flow relaxes back to its original state after the disturbances are removed.

Range II: $30° < \alpha < 60°$. In this incidence range the flow under normal conditions is usually asymmetric, but the level of the asymmetry depends on the amount of disturbances present on the tip of the body. It seems that the sensitivity of the flowfield increases as the disturbances are closer to the body apex, which suggests that the important parameter characterizing the effect of the disturbance is the ratio of the size of the disturbance to the local boundary layer thickness. In other words, the effect of a small disturbance near the apex will be much larger in comparison to the case where the same disturbance is placed on the aft part of the body. Since the tip of a wind-tunnel model represents a large collection of disturbances, the final effect is the sum of the contributions of all disturbances. As

a result, by changing the roll angle of the body different patterns may evolve (and even an almost symmetric pattern of the vortices may appear[9,19-20]). Apparently for laminar flows the most sensitive circumferential angles to place a disturbance are between 90° to 140° from the windward plane of symmetry[3,4,24]. In the present calculations perturbations were always placed at 90°.

Although the above mechanism gives a reasonable explanation for the behavior of the flowfield at this range of angles of attack, it fails in two main points. It does not explain why a small perturbation near the tip grows by several orders of magnitude as it convects downstream and it does not explain why the flowfield relaxes back to its original shape when the perturbation is removed (Fig. 1). The only mechanism which gives a satisfactory explanation to the whole is that of convective instability.

As mentioned earlier, the unsteady wake behind a two-dimensional cylinder is usually the result of an absolute instability, which means that any initial disturbance will grow in time and space. Due to nonlinear effects the growth of the disturbance will reach an equilibrium state and so the flow will evolve into a self-sustained oscillation of the wake (cf. Refs. 26-29). On the other hand, in the case of a convectively unstable wake (cf. Refs. 26,29,30,31), all disturbances will be carried away, leaving finally the wake undisturbed, unless the disturbance is maintained for all time, (e.g. as in the case of the 'vibrating ribbon'[32], or as was done in the case of the flow over a rotating disk[30]). From the rapid growth of the disturbances in the wake of the ogive-cylinder body and from the fact that upon removal of the geometrical disturbance or the jet, the wake relaxed back to the initial symmetric flowfield, it is suggested that the asymmetric flow which exists for this range of angles of attack is the result of disturbing a convectively unstable symmetric flow.

It also worth mentioning that from the calculations and from experimental observations[3,4] the flow over the growing part of the body (ie, the cone or the ogive forebody) is less asymmetric than that over the aft part of the body. This may explain why the experiments by Moskovitz et al.[24], which presented pressures measured on the nose only, show, relative to other experiments, smaller asymmetry for a given angle of attack. Also the effect of unsteady vortex shedding, which will be discussed next, could not be detected.

Range III: 60° < α ≤ 90°. As the angle of attack approaches 90° the flow in the wake of the body behaves in a manner similar to that of the Karman vortex shedding behind a two-dimensional circular cylinder. Experiments[3,4] showed that even for angles of attack lower than 70° vortices are shed in the wake of the cylindrical part of the body, and the Strouhal number varies with $\sin(\alpha)$, approaching the classical value for the two-dimensional cylinder as the angle of attack approaches 90°. This is also indicated by the numerical calculations presented here for $\alpha = 80°$. Such shedding is the result of an absolute instability, as explained above. The calculations presented here show that even for $\alpha = 60°$ the flow in the wake of the cylindrical part of the body can be shedding vortices if it is triggered by a short time perturbation (ie, as in the case of an absolute instability). On the other hand, in order to obtain the experimentally observed pair of asymmetric, steady vortices, which curved away from the tip, a space-fixed, permanent disturbance is needed. The latter

represents the result of convective instability of the symmetric flow. This result indicates that for certain angles of attack the flow around pointed, slender bodies may contain both instability mechanisms. The coexistence of the two instability mechanisms was also deduced by Yang and Zebib[29] from their computations for the unsteady wake behind a two-dimensional cylinder.

Acknowledgement

References

[1] Hunt, B. L., "Asymmetric Vortex Wakes on Slender Bodies," AIAA Paper 82-1336, August 1982.

[2] Ericsson, L. E. and Reding, J. P., "Aerodynamic Effects of Asymmetric Vortex Shedding from Slender Bodies," AIAA Paper 85-1797, August 1985.

[3] Degani, D. and Zilliac, G. G., "Experimental Study of Unsteadiness of the Flow Around an Ogive-Cylinder at Incidence," AIAA Paper 88-4330, August 1988.

[4] Degani, D. and Zilliac, G. G., "An Experimental Study of the Nonsteady Asymmetric Flow Around an Ogive-Cylinder at Incidence," AIAA Journal 28 (1990), pp. 642-649.

[5] Patel, V. A., "Karman Vortex Street behind a Circular Cylinder by the Series Truncation Method," J. Comp. Phys. 28 (1978), pp. 14-42.

[6] Lecointe, Y. and Piquet, J., "On the Use of Several Compact Methods for the Study of Unsteady Incompressible Viscous Flow Round a Circular Cylinder," Computers & Fluids 12 No. 4 (1984), 255-280.

[7] Rosenfeld, M., Kwak, D., and Vinokur, M., "A Solution Method for the Unsteady and Incompressible Navier-Stokes Equations in Generalized Coordinate Systems," AIAA Paper 88-0718, Jan. 1988.

[8] Tobak, M., Chapman, G. T., and Unal, A., "Modeling aerodynamic discontinuities and onset of chaos in flight dynamical systems," Annale des Telecommunications, Tome 42, No. 5-6, 1987.

[9] Lamont, P. J., "Pressures Around an Inclined Ogive-Cylinder With Laminar, Transitional, or Turbulent Separation," AIAA Journal 20 (1982), pp. 1492-1499.

[10] Keener, E. R. and Chapman, G. T., "Similarity in Vortex Asymmetric Flows Over Slender Bodies and Wings," AIAA Journal 15 (1988), pp. 1370-1372.

[11] Degani, D. and Schiff, L. B., "Numerical Simulation of Asymmetric Vortex Flows Occurring on Bodies of Revolution at Large Incidence," AIAA Paper 87-2628, August, 1987.

[12] Degani, D. and Schiff, L. B., "Numerical Simulation of the Effect of Spatial Disturbances on Vortex Asymmetry," AIAA Paper 89-0340, Jan. 1989.

[13] Degani, D. and Schiff, L. B., "Numerical Simulation of the Effect of Spatial Disturbances on Vortex Asymmetry," to appear, AIAA J., 1990.

[14] Steger, J. L., Ying, S. X., and Schiff, L. B., "A Partially Flux-Split Algorithm for Numerical Simulation of Unsteady Viscous Flows," Proceedings of a Workshop on Computational Fluid Dynamics, University of California, Davis, 1986.

[15] Viviand, H., "Conservative Forms of Gas Dynamics Equations," La Recherche Aerospatiale, No. 1, Jan–Feb (1974), 65–68.

[16] Baldwin, B. S. and Lomax, H., "Thin Layer Approximation and Algebraic Model for Separated Turbulent Flows," AIAA Paper 78–257, Jan. 1978.

[17] Steger, J. L., "Implicit Finite-Difference Simulation of Flow About Arbitrary Two-Dimensional Geometries," AIAA Journal 16 (1978), 679–686.

[18] Steger, J. L. and Warming, R. F., "Flux Vector Splitting of the Inviscid Gasdynamic Equations with Applications to Finite-Difference Methods," J. Comp. Phys. 40 (1981), 263–293.

[19] Hunt, B. L. and Dexter, P. C., "Pressures on a Slender Body at High Angle of Attack in a Very Low Turbulence Level Airstream," AGARD-CP-247, High Angle of Attack Aerodynamics, Paper 17, 1978.

[20] Dexter, P. C. and Hunt, B. L., "The Effects of Roll Angle on the Flow Over a Slender Body of Revolution at High Angle of Attack," AIAA 81-0358, Jan. 1981.

[21] Schiff, L. B., Degani, D. and Gavali, S., "Numerical Simulation of Vortex Unsteadiness on Slender Bodies of Revolution at Large Incidence," AIAA Paper 89-0195, Jan. 1989.

[22] Levy, Y., Seginer, A., and Degani, D., "Graphical Representation of Three-Dimensional Vortical Flows by Means of Helicity Density and Normalized Helicity," AIAA Paper 88-2598, June 1988.

[23] Levy, Y., Degani, D., and Seginer, A., "Graphical Representation of Three-Dimensional Vortical Flows by Means of Helicity," to appear, AIAA J., 1990.

[24] Moskovitz, C. A., Hall, R. M., and DeJarnette, F. R., "Effects of Nose Bluntness, Roughness and Surface Perturbations on the Asymmetric Flow Past Slender Bodies at Large Angles of Attack," AIAA Paper 88-2236CP, August 1989.

[25] Zilliac, G. G., Degani, D., and M. Tobak, "Asymmetric Vortices on a Slender Body of Revolution," AIAA Paper 90-0388, Jan. 1990.

[26] Triantafyllou, G. S., Kupfer, K., and Bers, A., "Absolute Instabilities and Self-Sustained Oscillation in the Wakes of Circular Cylinder," Physical Review Letters, 59, 1987, pp. 1014-1917.

[27] Chomaz, J. M., Huerre, P., and Redekopp, L. G., "Biforcations to Local and Global Modes in Spatially Developing Flows," Physical Review Letters, 60, 1988, pp. 25-28.

[28] Sreeninasan, K. R., Raghu, S., and Kyle, D., "Absolute Instability in Variable Density Round Jets," Experiments in Fluids, 7, 1989, pp. 309-317.

[29] Yang, X., and Zebib, A., "Absolute and Convective Instability of a Cylinder Wake," Physics of Fluids, 4, 1989, pp. 689-696.

[30] Wilkinson, S. P., and Malik, M. R., "Stability Experiments in the Flow over a Rotating Disk," AIAA J., 23, 1985, pp. 588-595.

[31] Gaster, M., "The Role of Spatially Growing Waves in the Theory of Hydrodynamic Stability," Progress in Aeronautical Sciences, 6, Ed. D. Kuchemann and L.H.G. Sterne, Pergamon Press, 1965.

[32] Schubauer, G. B., and Skramstad, H. K., "Laminar Boundary Layer Oscillations and Transition on a Flat Plate," NACA Report 909, 1949.
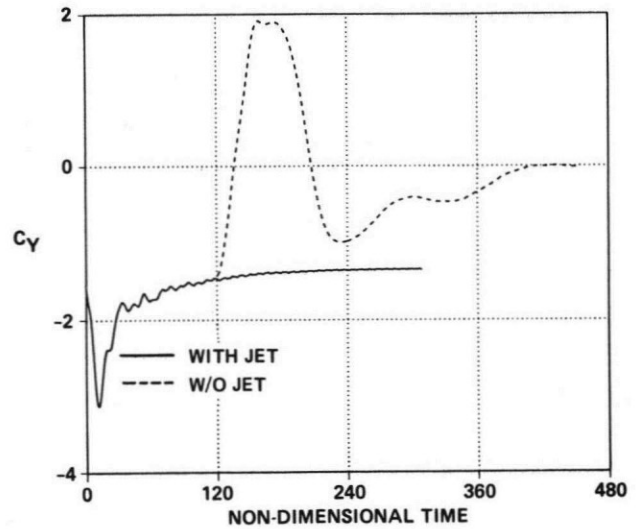
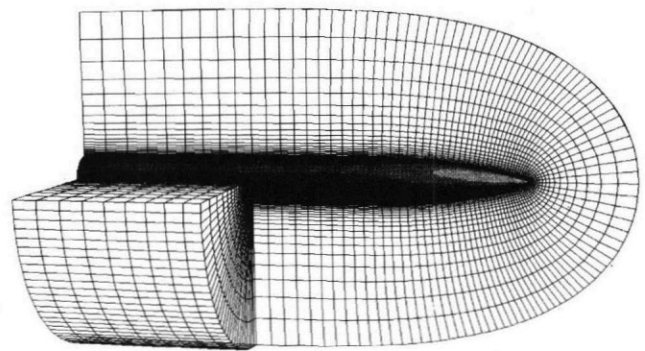**Fig. 1** Side-force coefficient history; $M_\infty = 0.2$, $\alpha = 40°$, $Re_D = 26,000$ (Ref. 13).
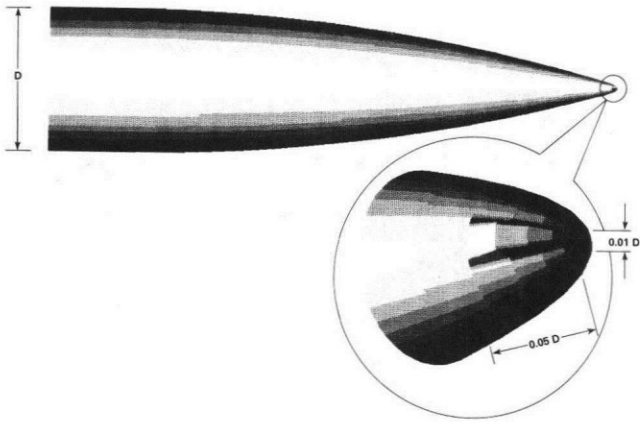

Fig. 2 Tangent ogive-cylinder grid.
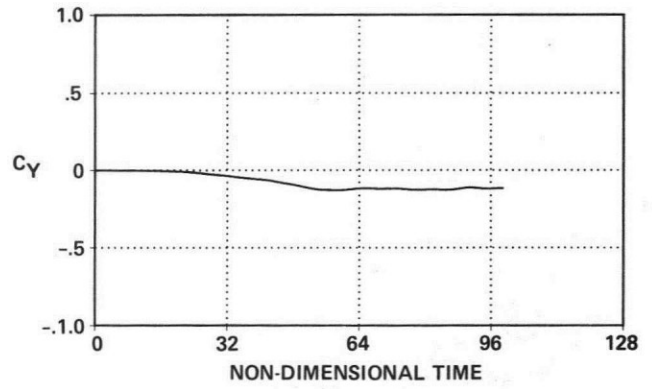
1167

Fig. 3 Geometrical disturbance.

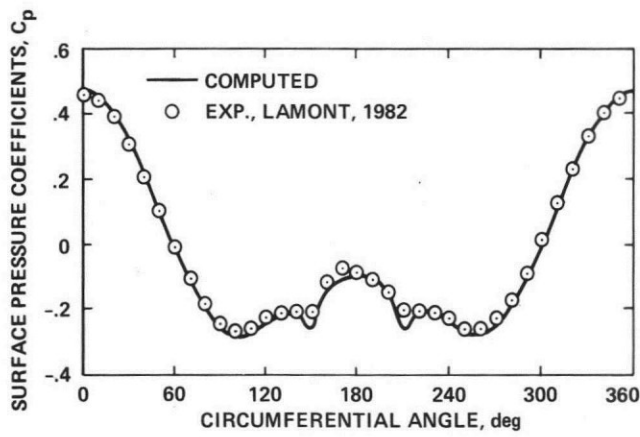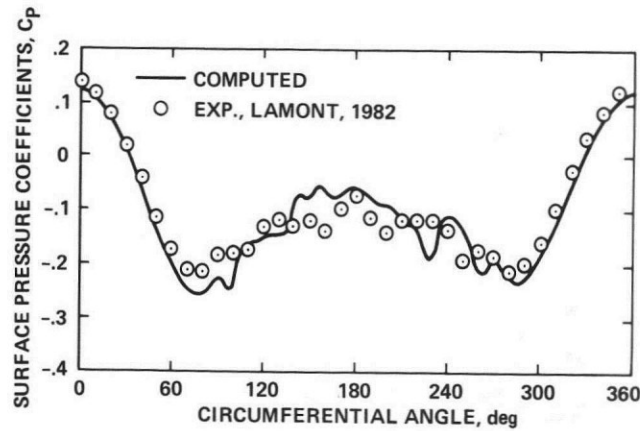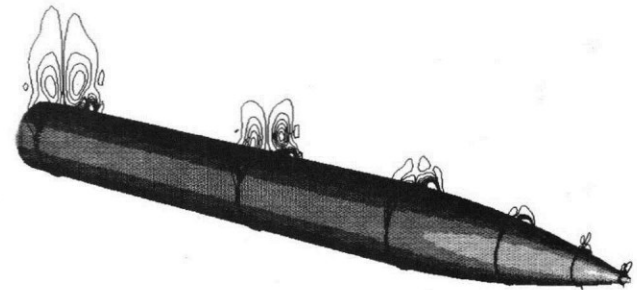**Fig. 5** Side-force coefficient history; h/D = 0.02, $M_\infty = 0.2$, $\alpha = 20°$, $Re_D = 200,000$.
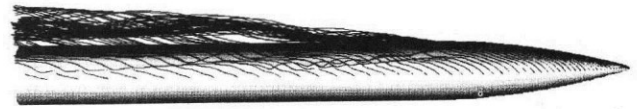

a) x/D = 0.5

b) x/D = 6.0

Fig. 4 Circumferential surface pressure distributions; h/D=0.02, $M_\infty = 0.2$, $\alpha = 20°$, $Re_D = 200,000$.

a) Helicity density contours.

b) Off-surface streamlines.

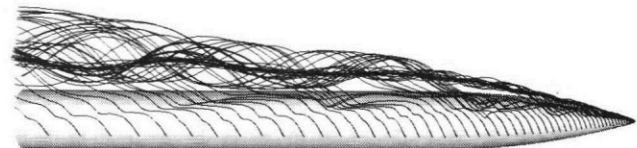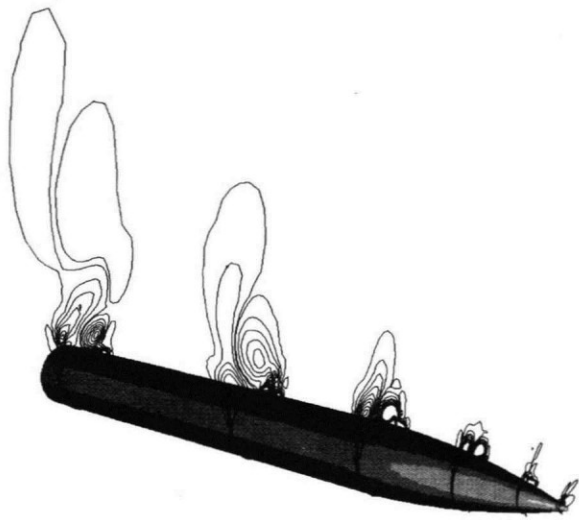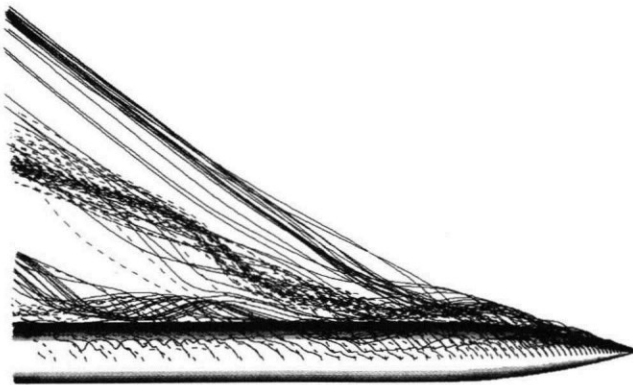**Fig. 6** Computational results (with geometrical disturbance) for h/D = 0.02, $M_\infty = 0.2$, $\alpha = 20°$, $Re_D = 200,000$.

Fig. 7 Off-surface streamlines - symmetric case; $\alpha = 40°$, $M_\infty = 0.2$, $Re_D = 200,000$.

a) Helicity density contours.

b) Off-surface streamlines.

Fig. 8 Computational results (with geometrical disturbance) for h/D = 0.01, $\alpha = 40°$, $M_\infty = 0.2$, $Re_D = 200,000$.
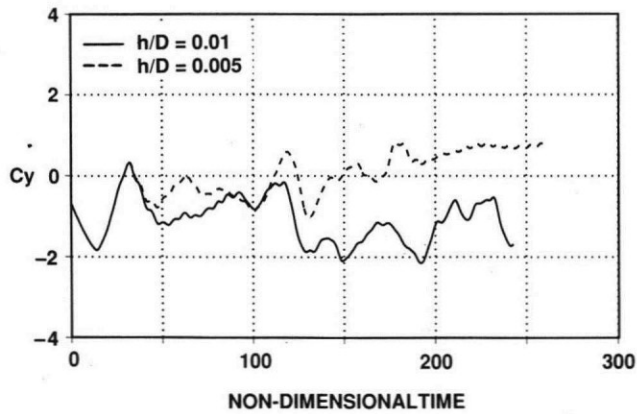
Fig. 9 Side-force coefficient history; $\alpha = 40°$, $M_\infty = 0.2$, $Re_D = 200,000$.
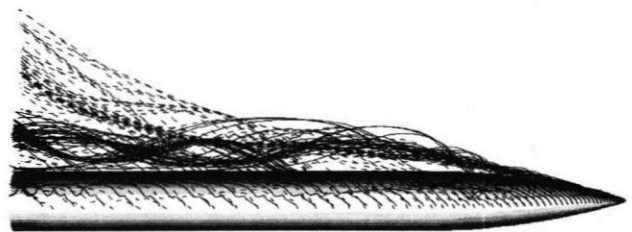
Fig. 10 Off-surface streamlines; h/D = 0.005, $M_\infty = 0.2$, $\alpha = 40°$, $Re_D = 200,000$.
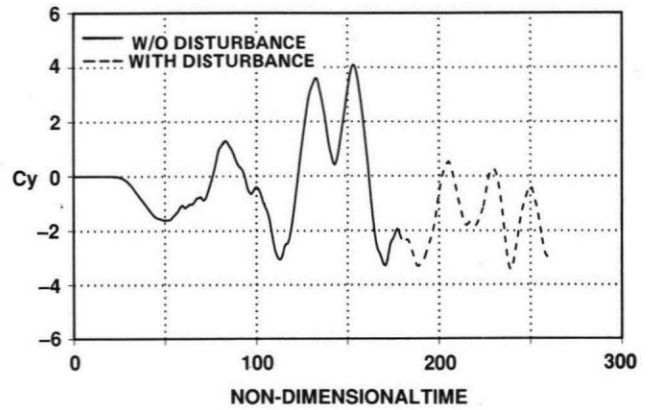
Fig. 11 Side-force coefficient history; $\alpha = 60°$, $M_\infty = 0.2$, $Re_D = 200,000$.
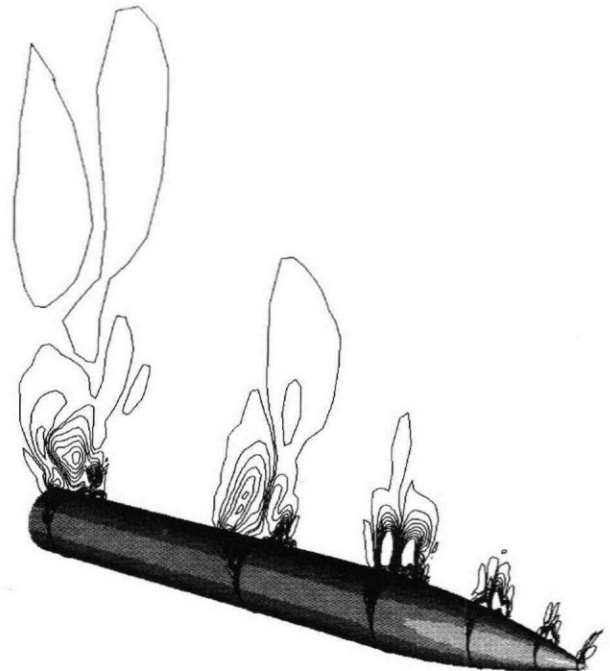
a) Helicity density contours.

Fig. 12 Computational results (without geometrical disturbance) for $\alpha = 60°$, $M_\infty = 0.2$, $Re_D = 200,000$.
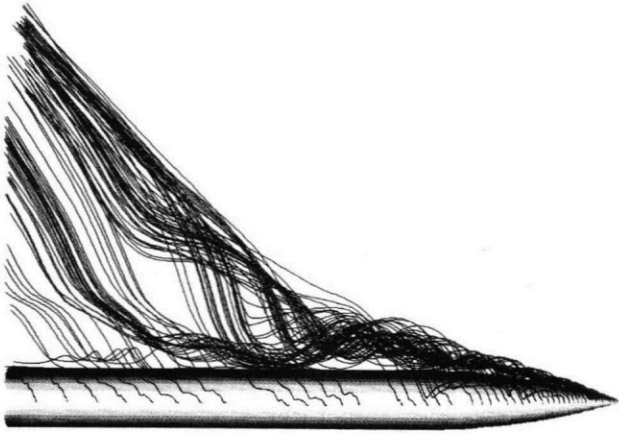
b) Off-surface streamlines.

Fig. 12 (Continued)
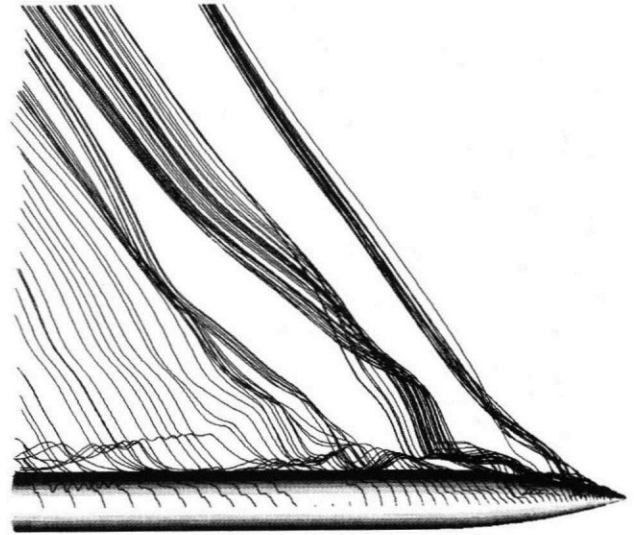
b) Off-surface streamlines.

Fig. 13 (Continued)
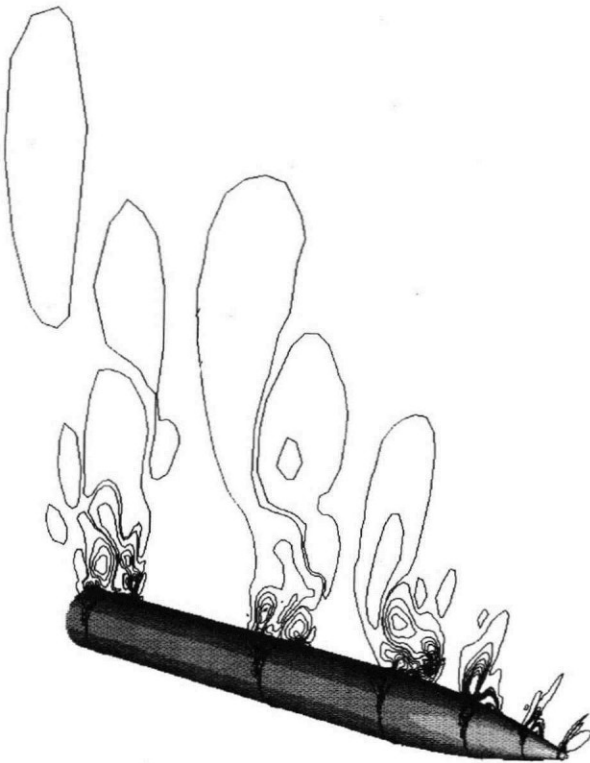
a) Helicity density contours.

Fig. 13 Computational results (with geometrical disturbance)
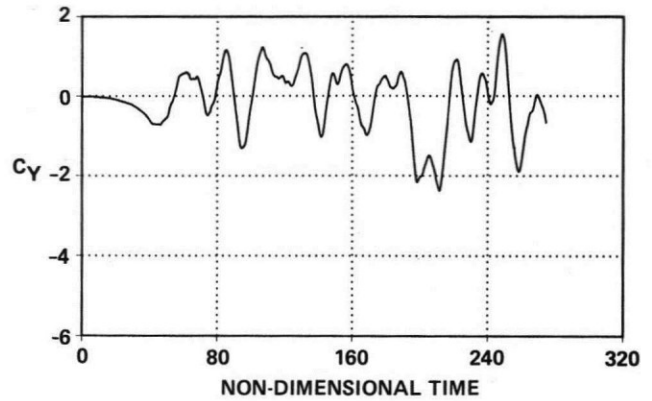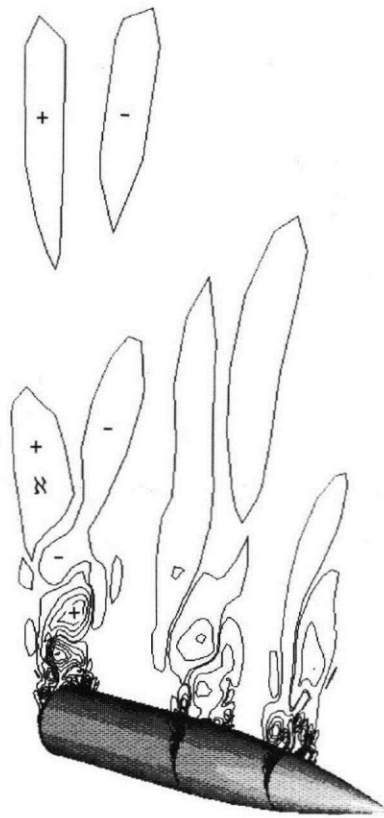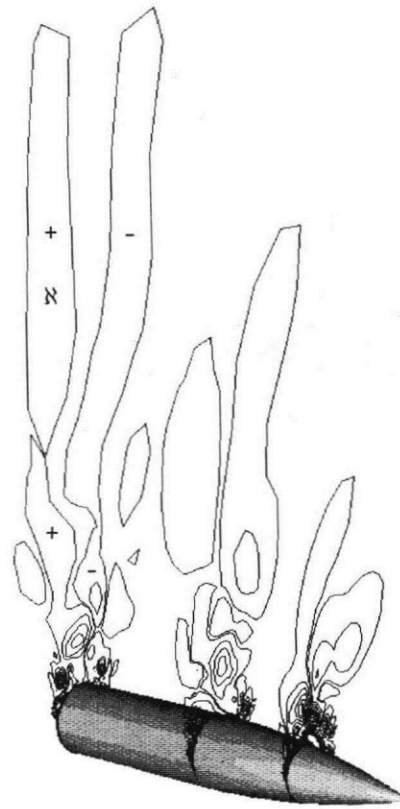for h/D = 0.01, $\alpha = 60°$, $M_\infty = 0.2$, Re$_D = 200,000$.

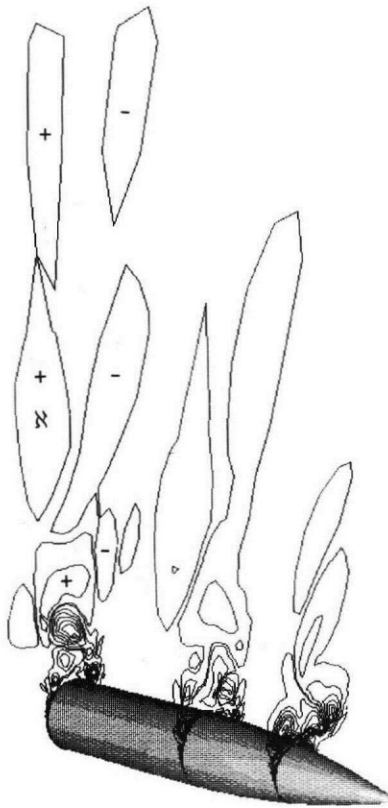Fig. 14 Side-force coefficient history; $\alpha = 80°$, $M_\infty = 0.2$,
Re$_D = 200,000$.

a) $\tilde{t} = \tilde{t}_\circ$

c) $\tilde{t} = \tilde{t}_\circ + 2\Delta\tilde{t}$

b) $\tilde{t} = \tilde{t}_\circ + \Delta\tilde{t}$
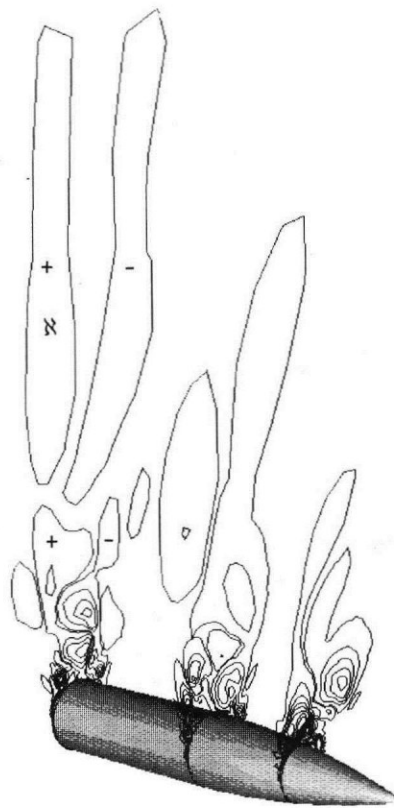
d) $\tilde{t} = \tilde{t}_\circ + 3\Delta\tilde{t}$

Fig. 15 Helicity density contours; $\alpha = 80°$, $M_\infty = 0.2$, $\mathrm{Re_D} = 200,000$.

a) $\tilde{t} = \tilde{t}_\circ$

b) $\tilde{t} = \tilde{t}_\circ + \Delta\tilde{t}$

c) $\tilde{t} = \tilde{t}_\circ + 2\Delta\tilde{t}$
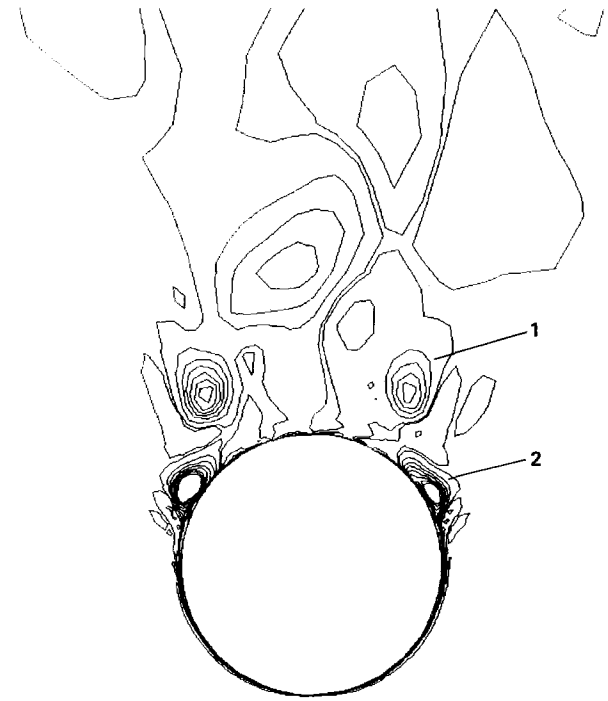
d) $\tilde{t} = \tilde{t}_\circ + 3\Delta\tilde{t}$

Fig. 16   Helicity density contours; x/D = 6.0, $\alpha = 80°$, $M_\infty = 0.2$, $Re_D = 200,000$.